IEEE Access
Multidisciplinary ⋮ Rapid Review ⋮ Open Access Journal

Received 5 June 2023, accepted 14 July 2023, date of publication 24 July 2023, date of current version 2 August 2023.

Digital Object Identifier 10.1109/ACCESS.2023.3298543

RESEARCH ARTICLE

Coupled Robust Constant-Power-Control Algorithm for Rigid Quadruple EMS Vehicle

ZEYI ZHANG
School of Electrical Engineering and Automation, Jiangxi University of Science and Technology, Ganzhou 341000, China
e-mail: zhangzy@jxust.edu.cn

This work was supported in part by the Science and Technology Research Project of Educational Department in Jiangxi Province under Grant GJJ210804, and in part by the High-Level Talents Research Start-Up Project of Jiangxi University of Science and Technology under Grant 205200100476.

ABSTRACT The electromagnetic-suspension (EMS) vehicle has been commercialized for the urban transportation in many countries. However, industrial applications of the small-size rigid quadruple counterpart are still restricted by the coupling problem or the so-called statically indeterminate problem among the four electromagnets. Inspired by the robust zero-power-control algorithm for the permanent-electromagnetic-suspension (PEMS) system, this work proposes the robust constant-power-control algorithm with the augmented integral controller to compensate the current coupling among the four electromagnets and to stabilize the rigid quadruple EMS vehicle. The proposed algorithm only involves three feedback control loops and four parameters. Detailed analytical derivations are addressed to determine the four parameters, whereas the numerical simulations are presented to demonstrate the effectiveness and the outstanding robustness of the proposed algorithm. Hence, the coupled robust constant-power-control algorithm significantly enhances the stability and reduces the complexity in the controller design as well as the mechanical structure for the rigid quadruple EMS vehicle. Also, the proposed algorithm is so simple that plenty of room is available to incorporate intelligent control algorithms. Consequently, this work sheds light on the intelligent EMS transportation system for more industrial applications.

INDEX TERMS Magnetic levitation, electromagnetic suspension, intelligent transportation systems, robust constant-power control.

I. INTRODUCTION

The electromagnetic suspension (EMS) is one of the magnetic levitation technologies [1]. And, the EMS transportation is famous for the zero friction, the strong climbing & turning ability, and the environment-friendly feature [2], so that it can satisfy harsh urban-transportation requirements and has been commercialized in many countries, such as Japan, Korea, and China. Moreover, the EMS transportation has vast industrial applications, such as for clean rooms [3], food or beverage factories [4], and noise-free environment [1].

Generally, the urban-transportation EMS vehicle is supported by several bogies, whereas each bogie has four sets of electromagnets and is separated into two rigid parts that are physically decoupled by the anti-roll beam [1], [2], [3]. Because of the difficulty in analyzing the coupling among the four electromagnets on the physically-decoupled EMS bogie, many studies in the literature only focused on the controller design for the single-degree-of-freedom (DoF) system, i.e., single set of electromagnet [4]. Lee et al. [5], Sinha and Pechev [6], Su et al. [7], and Suebsomran [8] optimized the dynamic performance of the single-DoF system with advanced control algorithms, such as the gain-scheduling control [5], the optimal control [6], the fuzzy control [7], and the neural network control [8], respectively.

Contrarily, industrial applications usually require the EMS vehicle to be small and rigid due to the tight budget of the structure and the maintenance. Mathematically, a rigid bogie with three sets of electromagnets formulates a statically determinate problem [9], [10], [11], whereas four sets of electromagnets with integral controllers (I controllers) are likely to over-constrain the rigid bogie and give rise to a

The associate editor coordinating the review of this manuscript and approving it for publication was Yanli Xu.

This work is licensed under a Creative Commons Attribution 4.0 License. For more information, see https://creativecommons.org/licenses/by/4.0/

statically indeterminate problem. In 2017, Yaseen [12] constructed a rigid quadruple EMS vehicle and observed an amplifying oscillation for the four separated proportional-integral-derivative controllers (PID controllers) and an attenuating oscillation for the four separated state-space feedback controllers without I controller. Also, the engineering tolerance [12], [13] and the track deflection [4] make it difficult to assign suitable floating-gap setpoints for the four separated I controllers. Therefore, the coupling among the four electromagnets potentially undermines the stability of the rigid quadruple EMS vehicle.

In the literature, there are generally two approaches to stabilize the rigid quadruple EMS vehicle against the statically indeterminate problem:

- *By a cross-coupling term*: in 2001, Park et al. [4] adopted the state-space feedback controller with the I controllers for the floating gaps and applied the cross-coupling term among the four electromagnets to stabilize the quadruple EMS vehicle.
- *By a minimum realization*: in 2003, Cruz et al. [14] overcame the statically-indeterminate problem by transforming the four floating-gap signals into the three position signals (i.e., *heave, pitch, and roll*) to formulate a minimum realization of the multi-input-multi-output (MIMO) close-loop system for the quadruple EMS vehicle.

However, the cross-coupling-term approach [4] involves augmented matrixes and tedious derivation due to the floating-gap I controllers. Besides, the minimum-realization approach [14] emphasizes on positions of the vehicle rather than the states of the electromagnets, which may undermine the robustness due to the exploitation of electromagnets. Therefore, the rigid quadruple EMS vehicle is still eager for a simple, robust and effective control algorithm.

Besides, the zero-power-control algorithm is famous for the permanent electromagnetic suspension (PEMS) system due to the biased magnetic force by the permanent magnet [15]. In 1988, Morishita and Azukizawa [16] applied the zero-power control to the small-size flexible quadruple PEMS vehicle with two rigid parts jointed by a shaft, whose mechanical structure was complex and like the bogie design for the EMS vehicle [1], [2], [3]. In 1994 and 1995, the robustness of the zero-power control was analyzed and examined by Tzeng and Wang [17], [18] for the single-DoF PEMS system. Later on, Mizuno and Takemori extended the realizations of the zero-power controller [15] and managed to apply the zero-power control to the PEMS bearing [19] and the PEMS vibration isolator [10]. In 2013, Cho et al. [13] succeeded in implementing the robust zero-power control for a rigid quadruple PEMS vehicle, but did not clarify the stabilizing mechanism among the four electromagnets. In 2020, Zhang et al. [20] analyzed the geometric modifications on the single-DoF PEMS system to enhance the zero-power-control performance.

Technically, the zero-power control improves the robustness of the PEMS system by the I controller to maintain the average value of the fluctuating excitation current at around zero and to enhance the stability under external disturbances [15], [18], which can be generalized as the constant-power control for the EMS system. This work proposes a coupled robust constant-power-control algorithm for the rigid quadruple EMS vehicle. Based on the double-loop constant-power controller design for the single-DoF EMS system and the current coupling of the quadruple EMS vehicle, the augmented I controller is designed to formulate a compensating loop to stabilize the four electromagnets against the statically indeterminate problem. The coupled algorithm involves only four parameters and is so simple that plenty of room is available to incorporate intelligent control algorithms, such as the optimal control, the gain-scheduling control, and the self-adaptive control.

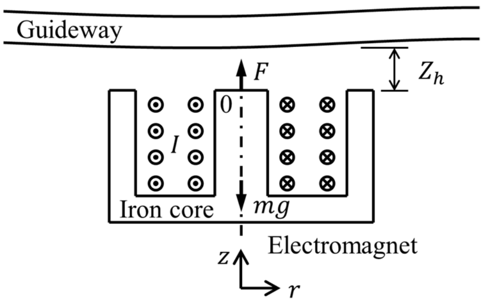

FIGURE 1. Sketch for the single-DoF EMS system consisting of the electromagnet and the ferrimagnetic guideway. The origin of the z-axis locates at the initial height of the upper surface of the electromagnet.

The paper starts with the theoretical work of the constant-power controller for the single-DoF EMS system in Sec. II, including (i) the kinetics analysis, (ii) the proportional-derivative controller (PD controller) for the distance loop, (iii) the I controller for the power loop, and (iv) the numerical simulation. Then, Sec. III analytically derives the coupled algorithm for the rigid quadruple EMS vehicle in four steps: (i) the kinetics analysis, (ii) the current coupling, (iii) the augmented I controller for the compensating loop, and (iv) the numerical simulation. Concluding remarks are addressed in Sec. IV.

II. SINGLE-DOF EMS SYSTEM

A. KINETICS ANALYSIS

Fig. 1 shows the single-DoF EMS system consisting of the electromagnet and the ferrimagnetic guideway. The z-axis is pointing vertically upwards and its origin locates at the initial height of the upper surface of the electromagnet. The electromagnet has a column shape and is restricted to move only along the z-axis. The excitation current, I, flows through the windings inside the electromagnet and generates a magnetic field to attract the ferrimagnetic guideway. The following two assumptions are adopted to simplify the magnetic field between the electromagnet and the guideway [21],

- The magnetic leakage is neglected;

- The magnetic reluctances of the iron core and the guideway are neglected compared with that of the air gap.

In Fig. 1, the floating gap is defined as the height difference between the guideway and the electromagnet,

$$Z_h = z_{\text{way}} - z_{\text{mag}} > 0, \tag{1}$$

where z_{way} measures the height of the lower surface of the guideway, and z_{mag} measures the height of the upper surface of the electromagnet. Taking second-order derivative of (1) about the time, t, leads to,

$$d^2Z_h \big/ dt^2 = a_{\text{way}} - a_{\text{mag}}, \tag{2}$$

where a stands for the vertical acceleration. Because z_{way} can be regarded as an external disturbance, the dominant dynamics of the single-DoF EMS system is,

$$d^2Z_h \big/ dt^2 = -a_{\text{mag}}. \tag{3}$$

The magnetic force between the guideway and the electromagnet can be modelled as the bi-variable function [8], [14] of I and Z_h as,

$$F = C \left(I/Z_h \right)^2, \tag{4}$$

where the electromagnet coefficient, C, involves the number of windings and the pole area.

Moreover, the force balance of the electromagnet gives,

$$F = m \left(g + a_{\text{mag}} \right), \tag{5}$$

where $m = 3$ kg is the mass of the electromagnet and $g = 10$ N/kg is the gravitational acceleration.

Hence, at the equilibrium with $a_{\text{mag}} = 0$, the equilibrium magnetic force is calculated from (4)-(5) as,

$$F_{eq} = C \left(I_{eq}/Z_{h,eq} \right)^2 = mg, \tag{6}$$

which indicates that the equilibrium excitation current is linearly proportional to the equilibrium floating gap, i.e., $I_{eq} \propto Z_{h,eq}$, for a constant payload, mg.

Since the electromagnet consumes the electric power to generate the magnetic force, it gets overheated when I exceeds certain value. Hence, we define the nominal excitation current, I_{norm}, as the excitation current for the electromagnet to work for a sufficiently long time without a significant temperature rise. Similarly, we define the nominal floating gap, $Z_{h,\text{norm}}$, for the nominal payload, F_{norm}, at I_{norm}, and this work adopts the following nominal parameters,

$$I_{\text{norm}} = 1.0 \text{ A}, Z_{h,\text{norm}} = 0.01 \text{ m}, \text{ and } F_{\text{norm}} = 30 \text{ N}, \tag{7}$$

whereas the electromagnet coefficient in (6) is solved as $C = F_{\text{norm}} \left(Z_{h,\text{norm}} / I_{\text{norm}} \right)^2 = 0.003 \text{ m}^2\text{N}/\text{A}^2$. Table 1 summarizes parameter values adopted in this work.

Furthermore, two types of working ranges are defined for the electromagnet regarding Z_h and I,

- *The tolerable ranges*: the mean values of Z_h and I should be within the tolerable ranges, i.e., ±20% about $Z_{h,\text{norm}}$ and ±50% about I_{norm},

$$Z_h \in (0.008, 0.012) \text{ m and } I \in (0.5, 1.5) \text{ A}, \tag{8}$$

whereas the mean magnetic force varies between 5.2 N and 105.5 N.

TABLE 1. **Parameter values.**

Symbol	Quantity	Value
I_{norm}	Nominal excitation current	1.0 A
$Z_{h,\text{norm}}$	Nominal floating gap	0.01 m
F_{norm}	Nominal payload	30 N
C	Electromagnet coefficient	0.003 m^{2}N/A^2
m	Electromagnet mass	3 kg
g	Gravitational acceleration	10 N/kg
k_P	Proportional gain for distance loop	-350 A/m
k_D	Derivative gain for distance loop	-6.5 A·s/m
k_I	Integral gain for power loop	0.033 m/(A·s)
K_{compen}	Integral gain (& compensating coefficient) for compensating loop	0.011 m/(A·s)

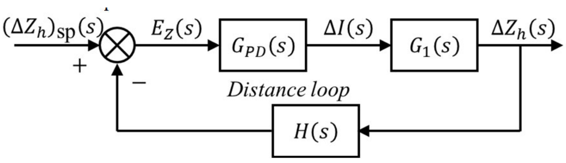

FIGURE 2. **Block diagram of the distance loop.**

- *The limit ranges*: the transient values of Z_h and I should be within the limit ranges, i.e., ±40% about $Z_{h,\text{norm}}$ and ±100% about I_{norm},

$$Z_h \in (0.006, 0.014) \text{ m and } I \in (0, 2.0) \text{ A}, \tag{9}$$

whereas the transient magnetic force varies between 0 N and 333.3 N.

Importantly, the single-DoF EMS system is regarded to lose control when both Z_h and I exceed the respective limit ranges.

Nevertheless, by imposing an infinitesimal perturbation, $\Delta Z_h = Z_h - Z_{h,eq}$, to the floating gap of the electromagnet, denote the current change as $\Delta I = I - I_{eq}$ and the force change as $\Delta F = F - F_{eq}$. Mathematically, ΔF in (4) is locally linearized about the equilibrium as [12], [22], and [23],

$$\Delta F = \frac{\partial F}{\partial I} \Delta I + \frac{\partial F}{\partial Z_h} \Delta Z_h = \frac{2CI_{eq}}{Z_{h,eq}^2} \Delta I - \frac{2CI_{eq}^2}{Z_{h,eq}^3} \Delta Z_h. \tag{10}$$

And, the dynamic equation is calculated from (3), (5), (6), and (10) as,

$$-\frac{d^2 Z_h}{dt^2} = 2g \left(\frac{\Delta I}{I_{eq}} - \frac{\Delta Z_h}{Z_{h,eq}} \right), \tag{11}$$

which gives the transfer function from ΔI to ΔZ_h by applying the Laplace transformation as,

$$G_1(s) = \frac{\Delta Z_h(s)}{\Delta I(s)} = \frac{-2g/I_{eq}}{s^2 - 2g/Z_{h,eq}}, \tag{12}$$

which is an unstable second-order system with a positive pole at $s = \sqrt{2g/Z_{h,eq}}$.

B. PD CONTROLLER FOR DISTANCE LOOP

In order to stabilize the single-DoF EMS system, i.e., $G_1(s)$, the negative feedback control is adopted and consists of the distance sensor, $H(s)$, and the PD controller, $G_{PD}(s)$, as shown in Fig. 2. For the ease of presentation, the distance sensor measures the floating gap, ΔZ_h, with a unity gain, i.e., $H(s) = 1$. And, the error signal of the distance loop is defined as,

$$E_Z(s) = (\Delta Z_h)_{\text{sp}}(s) - \Delta Z_h(s), \tag{13}$$

where $(\Delta Z_h)_{\text{sp}}$ is the floating-gap setpoint.

The transfer function of the PD controller for the distance loop is defined as,

$$G_{PD}(s) = \frac{\Delta I(s)}{E_Z(s)} = k_P + k_D s, \tag{14}$$

where k_P and k_D are the proportional gain and the derivative gain, respectively.

Therefore, the close-loop transfer function of the distance loop is,

$$\begin{aligned}\Phi_{\text{distance-loop}}(s) &= \frac{\Delta Z_h(s)}{(\Delta Z_h)_{\text{sp}}(s)} = \frac{G_{PD}(s)\,G_1(s)}{1 + H(s)\,G_{PD}(s)\,G_1(s)} \\ &= \frac{-2(k_P + k_D s)\,g/I_{eq}}{s^2 - (2k_D g/I_{eq})\,s - (2k_P g/I_{eq} + 2g/Z_{h,eq})},\end{aligned} \tag{15}$$

whose characteristic equation is,

$$s^2 - (2k_D g/I_{eq})\,s - (2k_P g/I_{eq} + 2g/Z_{h,eq}) = 0. \tag{16}$$

Moreover, the stability criterion requires positive coefficients for all terms in the above characteristic equation as,

$$\begin{cases} -k_D > 0 \\ -k_P > I_{eq}/Z_{h,eq} \end{cases}. \tag{17}$$

Technically, $|k_P|$ measures the proportional gain between ΔI and ΔZ_h, and is constrained by the power supply and the induction of the electromagnet. Also, a large $|k_P|$ is prone to amplify external disturbances. Hence, $|k_P|$ is preferred to be as small as possible and is determined by the maximum value of $(I_{eq}/Z_{h,eq})$ in the limit ranges as,

$$-k_P > \frac{I_{\max}}{Z_{h,\min}} = \frac{2}{0.006} = 333.3 \text{ A/m}. \tag{18}$$

Hence, $k_P = -350$ A/m is sufficient to stabilize the single-DoF EMS system in the limit ranges and is adopted in this work.

Furthermore, the characteristic equation in (16) can be transformed into a standard second-order form, i.e., $s^2 + 2\xi\omega_n s + \omega_n^2 = 0$, as,

$$\begin{cases} \xi\omega_n = -k_D g/I_{eq} \\ \omega_n^2 = -2k_P g/I_{eq} - 2g/Z_{h,eq} \end{cases}, \tag{19}$$

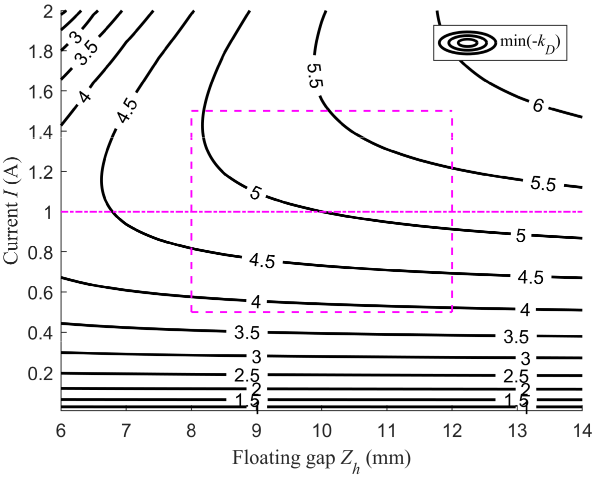

FIGURE 3. **Contour of min $(-k_D)$ in the limit ranges with $k_P = -350$ A/m. The contour with min $(-k_D) = 6.5$ A · s/m does not appear and becomes the necessary condition for (20) to be fulfilled for the whole limit ranges. The magenta dashed rectangle denotes the tolerable ranges, whereas the magenta dashed-dotted line denotes I_{norm}.**

where ξ is the damping ratio and ω_n is the natural frequency. Technically, we prefer $\xi \geq \sqrt{2}/2$, which leads to,

$$-k_D \geq \sqrt{-\frac{k_P I_{eq}}{g} - \frac{I_{eq}^2}{Z_{h,eq} g}}. \tag{20}$$

Fig. 3 visualizes the variation of $\min(-k_D) = \sqrt{-\frac{k_P I_{eq}}{g} - \frac{I_{eq}^2}{Z_{h,eq} g}}$ in the limit ranges with $k_P = -350$ A/m. Hence, by referring to Fig. 3, $k_D = -6.5$ A · s/m fulfils the requirement in (20) for the whole limit ranges. Note that the zero in $\Phi_{\text{distance-loop}}(s)$, i.e., $s = -k_P/k_D = -53.85$ s^{-1}, will influence the dynamics of the second-order system as well. Also, it is worth mentioning that the dynamics of the second-order system can be further optimized by the gain-scheduling algorithm for both $(-k_P)$ and $(-k_D)$.

Furthermore, the time constant of the second-order system is,

$$T_{\text{distance-loop}} = \frac{2\pi}{\omega_n} = \frac{2\pi}{\sqrt{-2k_P g/I_{eq} - 2g/Z_{h,eq}}}. \tag{21}$$

Fig. 4 visualizes the variation of $T_{\text{distance-loop}}$ in the limit ranges with $k_P = -350$ A/m. We observe that $T_{\text{distance-loop}}$ is smaller than 0.15 s in the tolerable ranges.

Nevertheless, the steady-state error of the distance loop in (13) under a unit step change in $(\Delta Z_h)_{\text{sp}}$, i.e., $(\Delta Z_h)_{\text{sp}}(s) = 1/s$, is calculated as,

$$\begin{aligned}\lim_{t\to\infty} e_Z(t) &= \lim_{s\to 0} sE_Z(s) = \lim_{s\to 0}\left(1 - \Phi_{\text{distance-loop}}(s)\right) \\ &= \frac{I_{eq}}{k_P Z_{h,eq} + I_{eq}} \neq 0.\end{aligned} \tag{22}$$

Hence, the PD controller for the distance loop cannot fully eliminate the steady-state error in ΔZ_h.

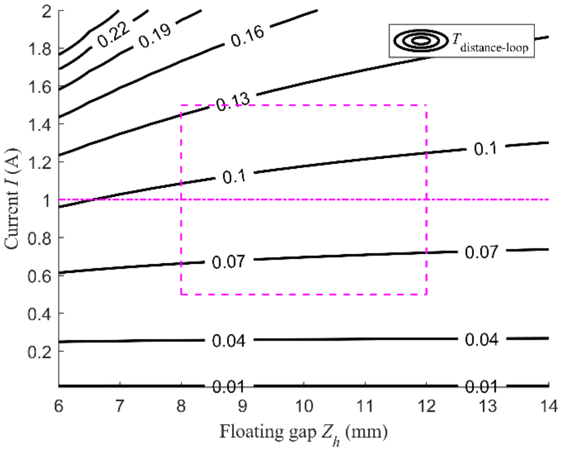

FIGURE 4. Contour of $T_{\text{distance-loop}}$ in the limit ranges with $k_P = -350$ A/m. The magenta dashed rectangle denotes the tolerable ranges, whereas the magenta dashed-dotted line denotes I_{norm}.

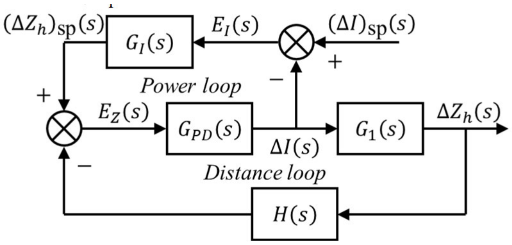

FIGURE 5. Block diagram of the distance loop and the power loop.

C. I CONTROLLER FOR POWER LOOP

In order to realize the constant-power control [15], another negative feedback control is adopted from the current change, ΔI, to the floating-gap setpoint, $(\Delta Z_h)_{\text{sp}}$, as shown in Fig. 5. In other words, the power loop aims to maintain I at I_{norm} by adjusting $(\Delta Z_h)_{\text{sp}}$.

Moreover, in order to prevent the power loop from affecting the transient dynamics of the distance loop, the time constant of the power loop is designed to be at least 10 times larger than that of the distance loop in the tolerable ranges as,

$$T_{\text{power-loop}} \geq 10 T_{\text{distance-loop}}. \tag{23}$$

Thus, solely considering the transient dynamics of the distance loop in Fig. 2, the close-loop transfer function from $(\Delta Z_h)_{\text{sp}}$ to ΔI is calculated as,

$$\begin{aligned}\Phi_{\text{current}}(s) &= \frac{\Delta I(s)}{(\Delta Z_h)_{\text{sp}}(s)} = \frac{G_{PD}(s)}{1 + H(s)\, G_{PD}(s)\, G_1(s)} \\ &= \frac{(k_P + k_D s)\left(s^2 - 2g/Z_{h,eq}\right)}{s^2 - \left(2k_D g/I_{eq}\right)s - \left(2k_P g/I_{eq} + 2g/Z_{h,eq}\right)}.\end{aligned} \tag{24}$$

Comparing with the much larger time constant of the power loop in (23), $\Phi_{\text{current}}(s)$ in the distance loop is approximated by its steady-state value,

$$G_2(s) = \frac{\Delta I(s)}{(\Delta Z_h)_{\text{sp}}(s)} = \lim_{s\to 0} \Phi_{\text{current}}(s) = \frac{k_P I_{eq}}{k_P Z_{h,eq} + I_{eq}}. \tag{25}$$

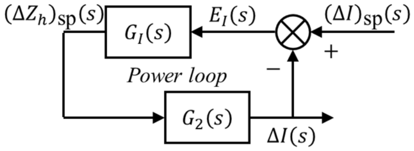

FIGURE 6. Block diagram of the power loop with the simplified distance loop.

Hence, Fig. 6 shows the block diagram of the power loop with the simplified distance loop by $G_2(s)$. The error signal of the power loop is defined as,

$$E_I(s) = (\Delta I)_{\text{sp}}(s) - \Delta I(s), \tag{26}$$

where $(\Delta I)_{\text{sp}}$ is the current setpoint.

The transfer function of the I controller for the power loop is,

$$G_I(s) = \frac{(\Delta Z_h)_{\text{sp}}(s)}{E_I(s)} = \frac{k_I}{s}, \tag{27}$$

where k_I is the integral gain.

Therefore, the close-loop transfer function of the power loop is,

$$\begin{aligned}\Phi_{\text{power-loop}}(s) &= \frac{\Delta I(s)}{(\Delta I)_{\text{sp}}(s)} = \frac{G_I(s)\, G_2(s)}{1 + G_I(s)\, G_2(s)} \\ &= \frac{1}{\frac{k_P Z_{h,eq} + I_{eq}}{k_I k_P I_{eq}} s + 1},\end{aligned} \tag{28}$$

whose time constant is,

$$T_{\text{power-loop}} = 2\pi \frac{k_P Z_{h,eq} + I_{eq}}{k_P I_{eq}} \frac{1}{k_I}. \tag{29}$$

The necessary condition of k_I is calculated from (23) and (29) as,

$$\frac{1}{k_I} \geq \frac{5}{\pi} \frac{k_P I_{eq}}{k_P Z_{h,eq} + I_{eq}} T_{\text{distance-loop}}. \tag{30}$$

Fig. 7 visualizes the variation of $\min\left(1/k_I\right) = \left(\frac{5}{\pi} \frac{k_P I_{eq}}{k_P Z_{h,eq} + I_{eq}} T_{\text{distance-loop}}\right)$ in the limit ranges with $k_P = -350\text{A/m}$. Hence, by referring to Fig. 7, $1/k_I = 30\text{A} \cdot \text{s/m}$ or $k_I = 0.033\text{m}/(\text{A} \cdot \text{s})$ fulfils the requirement in (30) for the whole tolerable ranges.

Nevertheless, the steady-state error of the power loop in (26) under a unit step change in $(\Delta I)_{\text{sp}}$, i.e., $(\Delta I)_{\text{sp}}(s) = 1/s$, is calculated as,

$$\lim_{t\to\infty} e_I(t) = \lim_{s\to 0} sE_I(s) = \lim_{s\to 0} \left(1 - \Phi_{\text{power-loop}}(s)\right) = 0. \tag{31}$$

Hence, the I controller for the power loop eliminates the steady-state error in ΔI.

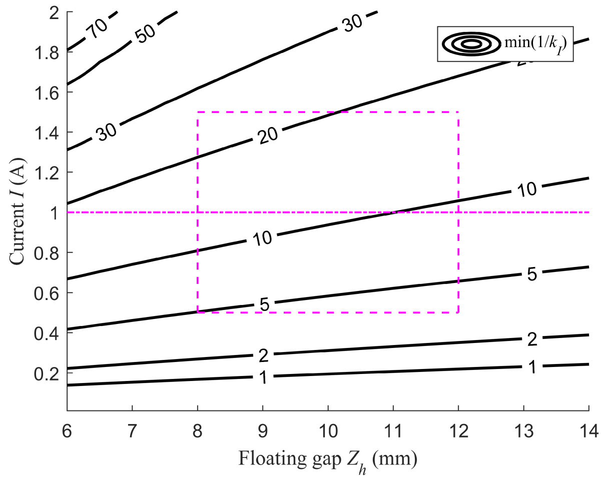

FIGURE 7. **Contour of min $(1/k_I)$ in the limit ranges with $k_P = -350$ A/m. The magenta dashed rectangle denotes the tolerable ranges, whereas the magenta dashed-dotted line denotes I_{norm}.**

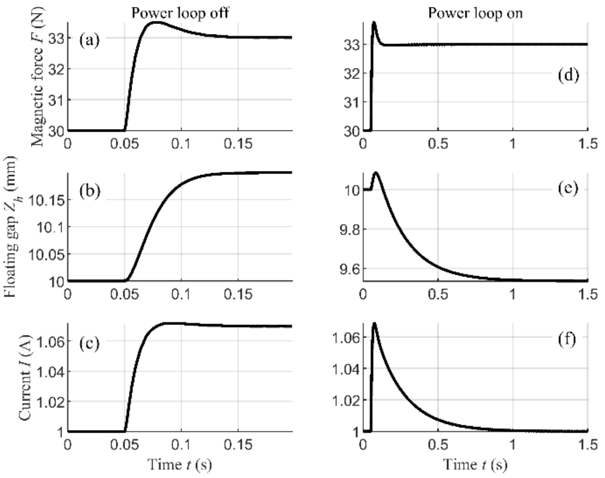

FIGURE 8. **Dynamic responses under a step change in mass on the single-DoF EMS system, (a-c) correspond to the single-loop scenario, whereas (d-f) correspond to the double-loop scenario.**

D. NUMERICAL SIMULATION

In this subsection, the numerical simulation is performed to compare the single-loop scenario and the double-loop scenario for the single-DoF EMS system. The MATLAB Simulink program is set up and shown in Fig. S1 (in supplementary materials). The program enables the step change in mass and the sinusoidal force disturbance. Also, the Gain between the distance-loop PD controller and the power-loop I controller in Fig. S1 switches between the single-loop scenario (Gain = 0) and the double-loop scenario (Gain = −1).

1) STEP CHANGE IN MASS

A step change in mass, $\Delta m = 0.3$ kg, is applied at $t = 0.05$ s to the nominal equilibrium, and the dynamic responses of the single-loop scenario and the double-loop scenario are compared.

Fig. 8 shows the dynamic responses under a step change in mass of F, Z_h, and I for the two scenarios. For the single-loop scenario, the transient process completes within 0.15 s. For the double-loop scenario, a quasi-static equilibrium is also achieved around $t = 0.15$ s in Fig. 8(d); during 0.15 s to 1.5 s, the I controller for the power loop continues bringing I back to I_{norm} and achieves the constant power by compensating $(\Delta Z_h)_{\text{sp}}$, while the magnetic force maintains at a constant value.

2) ROBUSTNESS TEST

In order to test the robustness of the constant-power control, two types of disturbances are imposed on the single-DoF EMS system as detailed below,

- *Step change in mass*: $\Delta m = 1.5$ kg is attached to the nominal mass at $t = 0.15$ s as,

$$\begin{cases} m(t) = m + \Delta m(t) \\ \Delta m(t) = \begin{cases} 0.0\text{ kg}, & 0.15\text{ s} > t \geq 0\text{ s} \\ 1.5\text{ kg}, & t \geq 0.15\text{ s}. \end{cases} \end{cases} \tag{32}$$

- *Sinusoidal force disturbance*: F_{d} has the same sign convention as the magnetic force, i.e., $F + F_{\text{d}} = m\left(g + a_{\text{mag}}\right)$. It has the frequency of 20 rad/s (i.e., the period of 0.31 s) and the ramping-up amplitude at the rate of 20 N/s since $t = 0.3$ s as,

$$\begin{cases} F_{\text{d}} = \text{ramp}(t)\sin(20t) \\ \text{ramp}(t) = \begin{cases} 0\text{ N}, & 0.3\text{ s} > t \geq 0\text{ s} \\ 20(t - 0.3)\text{ N}, & t \geq 0.3\text{ s}. \end{cases} \end{cases} \tag{33}$$

It is worth mentioning that the mass change is a low-frequency process, whereas the force disturbance is a high-frequency process. Specifically, the period of the force disturbance (0.31 s) is longer than the time constant of the distance loop (0.15 s) and shorter than the time constant of the power loop (1.5 s).

Fig. 9 shows the dynamic responses of the robustness test of F, Z_h, and I for the two scenarios. As shown in Fig. 9, the single-loop scenario reacts quickly (within 0.15 s) to the mass change and its equilibrium point shifts to (11.0 mm, 1.347 A); the double-loop scenario has the similar dynamic response to the single-loop scenario at the initial stage (within 0.15 s) but slowly (from 0.2 s to 0.4 s) converges to another equilibrium point at (8.16 mm, 1.0 A).

Moreover, Fig. 10 shows the corresponding $I - Z_h$ trajectories of the robustness test for the two scenarios. The two trajectories rotate around the respective centers, i.e., (11.0 mm, 1.347 A) for the single-loop scenario and (8.16 mm, 1.0 A) for the double-loop scenario. Besides, the two trajectories rotate within the respective narrow bands with a similar slope, i.e., $\Delta I = -k_P \Delta Z_h$, under the force disturbance. Hence, the proportional controller (P controller) for the distance loop dominates the transient dynamics due to its small time constant.

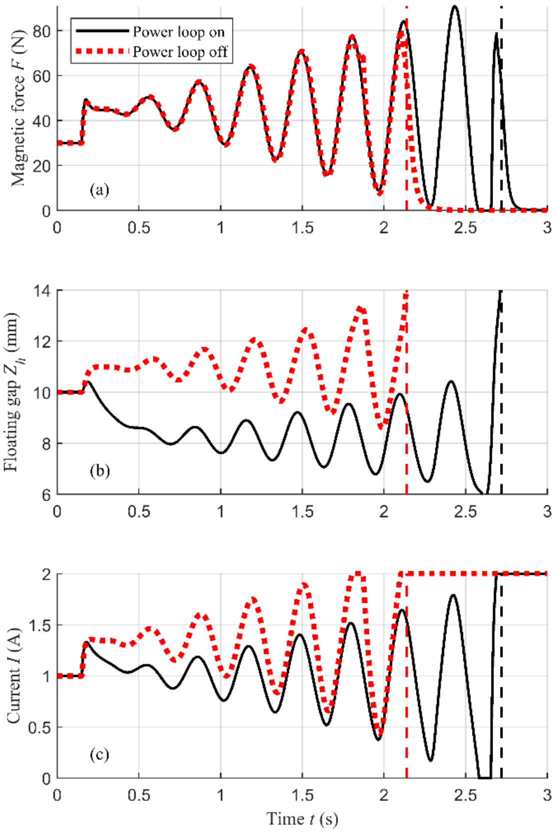

FIGURE 9. Dynamic responses of the robustness test on the single-DoF EMS system under two scenarios, (a) magnetic force, (b) floating gap, and (c) excitation current.

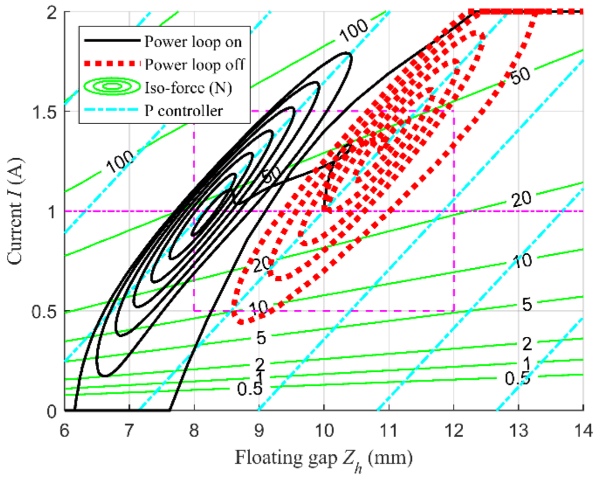

FIGURE 10. $I - Z_h$ trajectories of the robustness test on the single-DoF EMS system under two scenarios. The iso-force curves indicate the magnitudes of the magnetic force, whereas the P-controller lines indicate the dominant transient dynamics.

Furthermore, we observe from Fig. 9 that the single-loop scenario loses control when both I and Z_h exceed the respective upper limits at around $t = 2.14$ s, whereas the double-loop scenario loses control at around $t = 2.72$ s. The delay in the loss of control for the double-loop scenario results from the I controller for the power loop, which maintains the average value of I at I_{norm}. On the contrary, the single-loop scenario only relies on the PD controller for the distance loop and its I significantly deviates from I_{norm} upon the mass change, which accelerates the loss of control under the later sinusoidal force disturbance.

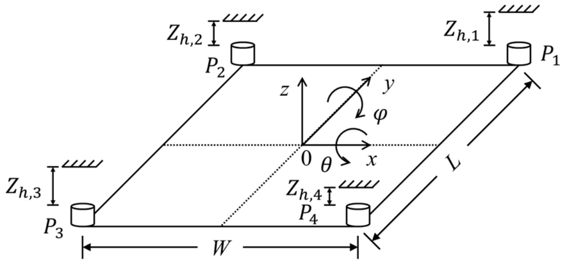

FIGURE 11. Structure of the rigid quadruple EMS vehicle. The four electromagnets locate on the four corners, whereas the origin locates at the center of the vehicle. The bogie has the width of $W = 0.6$ m along the x-axis and the length of $L = 0.5$ m along the y-axis.

Consequently, the I controller for the power loop can digest the low-frequency disturbance, e.g., Δm, whereas the PD controller for the distance loop can stabilize the high-frequency disturbance, e.g., F_{d}. Therefore, the double-loop scenario is more robust than the single-loop scenario and is highly promising for the rigid quadruple EMS vehicle.

III. RIGID QUADRUPLE EMS VEHICLE

In this section, we explore the coupled robust constant-power-control algorithm for the rigid quadruple EMS vehicle by analytical derivation and numerical simulation.

A. KINETICS ANALYSIS

As shown in Fig. 11, the rigid quadruple EMS vehicle consists of four electromagnets on the four corners, whereas the origin locates at the center of the vehicle. The bogie has the width of $W = 0.6$ m along the x-axis and the length of $L = 0.5$ m along the y-axis. Also, we adopt the following assumptions,

- The guideway and the bogie are rigid;
- The mass distribution of the electromagnet is uniform and its center of mass locates at its geometric center;
- In order to focus on the interactions between the guideway and the four electromagnets, the mass of the rigid bogie is neglected compared with the four electromagnets. Moreover, the influence from the bogie mass is detailed in Appendix;
- The four electromagnets are identical and share the same nominal parameters in Table 1.

In this work, three degrees of freedom are considered for the rigid bogie [11] including,

- The heaving translation, $z_B(t)$, along the z-axis;
- The rolling rotation, $\varphi_B(t)$, about the y-axis; and
- The pitching rotation, $\theta_B(t)$, about the x-axis.

Besides, the above three degrees of freedom are also adopted by the minimum-realization approach [14].

The other three degrees of freedom are out of the scope of this work because they cannot be directly driven by the magnetic forces between the guideway and the four electromagnets [4], [16], and they are,

- The translation along the x-axis;
- The translation along the y-axis; and
- The rotation about the z-axis.

In Fig. 11, the coordinates of the four electromagnets are denoted as [14],

$$\begin{cases} P_1 = \left(\frac{W}{2}, \frac{L}{2}, z_{\text{mag},1}\right) \\ P_2 = \left(-\frac{W}{2}, \frac{L}{2}, z_{\text{mag},2}\right) \\ P_3 = \left(-\frac{W}{2}, -\frac{L}{2}, z_{\text{mag},3}\right) \\ P_4 = \left(\frac{W}{2}, -\frac{L}{2}, z_{\text{mag},4}\right) \end{cases}. \tag{34}$$

Moreover, the z coordinates of the four electromagnets have the geometric relationships with the bogie as follows,

$$\begin{cases} z_{\text{mag},1} = z_B - \frac{W}{2}\sin\varphi_B + \frac{L}{2}\sin\theta_B \\ z_{\text{mag},2} = z_B + \frac{W}{2}\sin\varphi_B + \frac{L}{2}\sin\theta_B \\ z_{\text{mag},3} = z_B + \frac{W}{2}\sin\varphi_B - \frac{L}{2}\sin\theta_B \\ z_{\text{mag},4} = z_B - \frac{W}{2}\sin\varphi_B - \frac{L}{2}\sin\theta_B \end{cases}, \tag{35}$$

where z_B is the height of the bogie gravity center.

The force balance of the rigid bogie gives,

$$F_1 + F_2 + F_3 + F_4 = 4m\,(g + a_B)\,, \tag{36}$$

where $4m$ is the total mass of the bogie, $a_B = d^2 z_B / dt^2$ is the acceleration of the bogie gravity center, and $F_i = C\left(I_i / Z_{h,i}\right)^2 \geq 0$ with $i = 1, 2, 3$ and 4 are the magnetic forces between each electromagnet and the guideway.

The moment balance of the bogie gives,

$$\begin{cases} \frac{L}{2}\left(F_1 + F_2 - F_3 - F_4\right) = J_{xx}\frac{d^2\theta_B}{dt^2} \\ \frac{W}{2}\left(-F_1 + F_2 + F_3 - F_4\right) = J_{yy}\frac{d^2\varphi_B}{dt^2} \end{cases}, \tag{37}$$

where $J_{xx} = mL^2$ is the moment of inertia about the x-axis and $J_{yy} = mW^2$ is the moment of inertia about the y-axis.

Under the steady-state condition, F_i are calculated from (36)-(37) as,

$$\begin{cases} F_1 = F_3 \\ F_2 = F_4 \\ F_1 + F_2 = F_3 + F_4 = 2mg \end{cases}, \tag{38}$$

whose number of unknowns is more than the number of equations. Hence, (38) is an under-constrained equation set and requires additional condition(s) to ensure the uniqueness.

Furthermore, though the rigid bogie has the ideal structure, the guideway deflects due to engineering errors [4], [12], [13]. Denote the deflections of the guideway on the four electromagnets as ee_i with $i = 1, 2, 3$ and 4, and the four floating gaps are denoted as,

$$Z_{h,i} = z_{\text{way}} + ee_i - z_{\text{mag},i}. \tag{39}$$

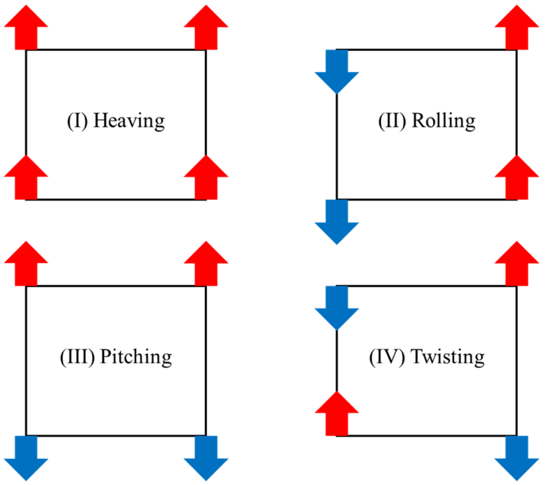

FIGURE 12. **Four eigen modes for the four floating gaps under the top view, (I) the heaving mode along the z-axis, (II) the rolling mode about the y-axis, (III) the pitching mode about the x-axis, and (IV)the twisting mode. Red-upwards and blue-downwards arrows stand for +1 and -1 respectively for the sign convention of the eigen modes along the z-axis.**

Mathematically, the four floating gaps are decomposed into the following four eigen modes, as shown in Fig. 12,

I. The heaving mode along the z-axis,

$$\left(Z_{h,1}, Z_{h,2}, Z_{h,3}, Z_{h,4}\right)_{\text{I}} = \frac{1}{4}\sum\left(z_{\text{way}} + ee_i - z_{\text{mag},i}\right)(1, 1, 1, 1)\,. \tag{40}$$

II. The rolling mode about the y-axis,

$$\left(Z_{h,1}, Z_{h,2}, Z_{h,3}, Z_{h,4}\right)_{\text{II}} = \frac{1}{4}\left[\sum\nolimits_{1,4}\left(ee_i - z_{\text{mag},i}\right) - \sum\nolimits_{2,3}\left(ee_i - z_{\text{mag},i}\right)\right](1, -1, -1, 1)\,. \tag{41}$$

III. The pitching mode about the x-axis,

$$\left(Z_{h,1}, Z_{h,2}, Z_{h,3}, Z_{h,4}\right)_{\text{III}} = \frac{1}{4}\left[\sum\nolimits_{1,2}\left(ee_i - z_{\text{mag},i}\right) - \sum\nolimits_{3,4}\left(ee_i - z_{\text{mag},i}\right)\right](1, 1, -1, -1)\,. \tag{42}$$

IV. The twisting mode,

$$\left(Z_{h,1}, Z_{h,2}, Z_{h,3}, Z_{h,4}\right)_{\text{IV}} = \frac{1}{4}\left[\sum\nolimits_{1,3}\left(ee_i - z_{\text{mag},i}\right) - \sum\nolimits_{2,4}\left(ee_i - z_{\text{mag},i}\right)\right](1, -1, 1, -1)\,. \tag{43}$$

Importantly, the first three eigen modes, i.e., (i) the heaving mode, (ii) the rolling mode, and (iii) the pitching mode, can be respectively compensated by the three basic motions of the rigid bogie, i.e., (i) the heaving translation, (ii) the rolling rotation, and (iii) the pitching rotation, without affecting the steady-state value of $Z_{h,i}$ or I_i for the four electromagnets.

Contrarily, the twisting mode results in nontrivial changes in both $Z_{h,i}$ and I_i for the four electromagnets. Assume the twisting-mode deflection of the guideway is $ee_1 = -ee_2 = ee_3 = -ee_4 = \Delta$. Due to the symmetry, the rigid bogie maintains horizontal with $z_{\mathrm{mag},1} = z_{\mathrm{mag},2} = z_{\mathrm{mag},3} = z_{\mathrm{mag},4}$. Hence, the four floating gaps are,

$$\left(Z_{h,1}, Z_{h,2}, Z_{h,3}, Z_{h,4}\right) = (\Delta, -\Delta, \Delta, -\Delta) + Z_{h,B}, \quad (44)$$

where $Z_{h,B} = z_{\mathrm{way}} - z_B$ denotes the average floating gap.

Nevertheless, the governing equation is derived from (4), (38), and (44) with three unknowns, I_1, I_2, and $Z_{h,B}$,

$$F_1 + F_2 = C\left(\frac{I_1}{Z_{h,B} + \Delta}\right)^2 + C\left(\frac{I_2}{Z_{h,B} - \Delta}\right)^2 = 2mg, \quad (45)$$

which can be solved together with the transfer functions between I_i and $Z_{h,i}$, i.e., the single-loop scenario or the double-loop scenario. Therefore, the rigid quadruple EMS vehicle has different equilibrium floating gaps under different control algorithms, which is presented in Sec. III-D.1.

B. CURRENT COUPLING

Mathematically, for a triple EMS vehicle, the force on each electromagnet can be independently determined by the force and moment balance analysis, e.g., (36)-(37), so that the setpoint change of an electromagnet will not influence other electromagnets [11]. However, for a rigid quadruple EMS vehicle, the four electromagnets are tightly coupled with each other, which requires a proper compensating algorithm to coordinate each other [13]. This subsection analyzes the current coupling among the four electromagnets.

Assume the rigid quadruple EMS vehicle is initially stabilized at the nominal equilibrium by four independent PD controllers in (14) without the power loop. Then, without loss of generality, the floating-gap setpoint of P_1 is increased by an infinitesimal amount, i.e., $(\Delta Z_h)'_{\mathrm{sp},1} = (\Delta Z_h)_{\mathrm{sp},1} + (\delta Z_h)_{\mathrm{sp},1}$. At the new equilibrium due to $(\delta Z_h)_{\mathrm{sp},1}$, denote the changes of the excitation currents, the floating gaps, and the magnetic forces of the four electromagnets as δI_i, $\delta Z_{h,i}$, and δF_i, respectively, with respect to (w.r.t.) the nominal equilibrium.

By applying the force and moment balances in (38), the relationships among the four force changes are,

$$\delta F_1 = -\delta F_2 = \delta F_3 = -\delta F_4. \quad (46)$$

Moreover, due to the P controller in (14) and the unchanged $(\Delta Z_h)_{\mathrm{sp},i}$ with $i = 2, 3$ and 4, the respective relationships between δI_i and $\delta Z_{h,i}$ are,

$$\delta I_i = -k_P \delta Z_{h,i} \text{ with } i = 2, 3 \text{ and } 4. \quad (47)$$

Besides, considering $(\delta Z_h)_{\mathrm{sp},1}$, the relationship between δI_1 and $\delta Z_{h,1}$ is,

$$\delta I_1 = k_P\left[(\delta Z_h)_{\mathrm{sp},1} - \delta Z_{h,1}\right]. \quad (48)$$

Furthermore, by applying (47) to (10), the relationships between $\delta Z_{h,i}$ and δF_i are derived as,

$$\delta F_i = -\left(k_P \frac{2CI_{eq}}{Z_{h,eq}^2} + \frac{2CI_{eq}^2}{Z_{h,eq}^3}\right)\delta Z_{h,i} \text{ with } i = 2, 3 \text{ and } 4. \quad (49)$$

Hence, combining (46) and (49) leads to,

$$\delta Z_{h,2} = -\delta Z_{h,3} = \delta Z_{h,4}. \quad (50)$$

Since the bogie is rigid, $\delta Z_{h,1}$ is solved from (35) and (50) as,

$$\delta Z_{h,1} = 3\delta Z_{h,2}. \quad (51)$$

Also, by applying (48) to (10), the relationship between $\delta Z_{h,1}$ and δF_1 is derived as,

$$\delta F_1 = k_P \frac{2CI_{eq}}{Z_{h,eq}^2}(\delta Z_h)_{\mathrm{sp},1} - \left(k_P \frac{2CI_{eq}}{Z_{h,eq}^2} + \frac{2CI_{eq}^2}{Z_{h,eq}^3}\right)\delta Z_{h,1}. \quad (52)$$

Therefore, the relationships among $\delta Z_{h,i}$ and $(\delta Z_h)_{\mathrm{sp},1}$ are derived from (46) and (49)-(52) as,

$$\begin{aligned}\frac{1}{3}\delta Z_{h,1} &= \delta Z_{h,2} = -\delta Z_{h,3} = \delta Z_{h,4} \\ &= \frac{k_P Z_{h,eq}}{4\left(k_P Z_{h,eq} + I_{eq}\right)}(\delta Z_h)_{\mathrm{sp},1}\,, \end{aligned} \quad (53)$$

where the coefficient $k_P / 4\left(k_P + I_{eq}/Z_{h,eq}\right) > 0$ varies with $I_{eq}/Z_{h,eq}$ for different equilibrium points.

Nevertheless, δI_i is solved from (47), (48), and (53) as,

$$\begin{cases} \delta I_1 = \frac{k_P^2 Z_{h,eq} + 4k_P I_{eq}}{4(k_P Z_{h,eq} + I_{eq})}(\delta Z_h)_{\mathrm{sp},1} \\ \delta I_2 = -\delta I_3 = \delta I_4 = \frac{-k_P^2 Z_{h,eq}}{4(k_P Z_{h,eq} + I_{eq})}(\delta Z_h)_{\mathrm{sp},1} \end{cases}, \quad (54)$$

where the coefficient of δI_1, i.e., $k_P\left(k_P + 4\frac{I_{eq}}{Z_{h,eq}}\right) \Big/ 4\left(k_P + \frac{I_{eq}}{Z_{h,eq}}\right)$, could be positive or negative depending on $I_{eq}/Z_{h,eq}$. Specifically, at the nominal equilibrium, $\delta I_1 = 17.5\,(\delta Z_h)_{\mathrm{sp},1}$ and $\delta I_2 = -\delta I_3 = \delta I_4 = 122.5\,(\delta Z_h)_{\mathrm{sp},1}$, which implies that $|\delta I_1|$ is much smaller than other $|\delta I_i|$ even though $(\delta Z_h)_{\mathrm{sp},1}$ is imposed on P_1.

Additionally, the difference between $(\delta I_1 + \delta I_3)$ and $(\delta I_2 + \delta I_4)$ is calculated as,

$$(\delta I_1 + \delta I_3) - (\delta I_2 + \delta I_4) = k_P\,(\delta Z_h)_{\mathrm{sp},1}\,. \quad (55)$$

Consequently, ΔI_i of the four electromagnets in the rigid quadruple EMS vehicle couple with each other which leads to the statically indeterminate problem, whereas the change of floating-gap setpoints potentially diverges $(\Delta I_1 + \Delta I_3)$ and $(\Delta I_2 + \Delta I_4)$ and leads to instability. The numerical simulation is presented in Sec. III-D.1 to verify the derived current coupling.

C. AUGMENTED I CONTROLLER FOR COMPENSATING LOOP

Sec. III-B models the current coupling among the four electromagnets by imposing an infinitesimal change to one floating-gap setpoint and shows that the setpoint change may increase the discrepancy between $(\Delta I_1 + \Delta I_3)$ and $(\Delta I_2 + \Delta I_4)$. In order to compensate the current coupling associated with the power loop, this subsection proposes an augmented I controller to formulate a compensating loop for the rigid quadruple EMS vehicle, as shown in Fig. 13.

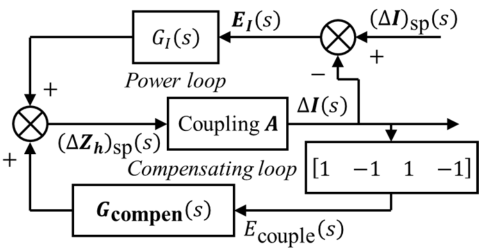

FIGURE 13. Block diagram of the compensating loop and the power loop. The coefficient matrix *A* involves the current coupling and the simplified distance loop.

Assume the rigid quadruple EMS vehicle is initially stabilized at the nominal equilibrium by four independent PD controllers. By generalizing (54), the coupling among $(\Delta Z_h)_{\mathrm{sp},i}$ and ΔI_i is derived as,

$$\boldsymbol{\Delta I} = \frac{k_P Z_{h,eq}}{4\left(k_P Z_{h,eq}+I_{eq}\right)}\left\{\frac{4I_{eq}}{Z_{h,eq}}\begin{bmatrix}1&0&0&0\\0&1&0&0\\0&0&1&0\\0&0&0&1\end{bmatrix} + k_P\begin{bmatrix}1&-1&1&-1\\-1&1&-1&1\\1&-1&1&-1\\-1&1&-1&1\end{bmatrix}\right\}(\Delta \boldsymbol{Z_h})_{\mathrm{sp}} = \boldsymbol{A}\,(\Delta \boldsymbol{Z_h})_{\mathrm{sp}}, \tag{56}$$

where $\boldsymbol{\Delta I} = \left[\Delta I_1\ \Delta I_2\ \Delta I_3\ \Delta I_4\right]^T$ is the current-change vector, $(\Delta \boldsymbol{Z_h})_{\mathrm{sp}} = \left[(\Delta Z_h)_{\mathrm{sp},1}\ (\Delta Z_h)_{\mathrm{sp},2}\ (\Delta Z_h)_{\mathrm{sp},3}\ (\Delta Z_h)_{\mathrm{sp},4}\right]^T$ is the setpoint-change vector, and $\boldsymbol{A}$ is the coupling matrix between $(\Delta \boldsymbol{Z_h})_{\mathrm{sp}}$ and $\boldsymbol{\Delta I}$.

Also, the error signal of the compensating loop is denoted as,

$$\begin{aligned}E_{\mathrm{couple}}(s) &= \left[\Delta I_1(s)+\Delta I_3(s)\right]-\left[\Delta I_2(s)+\Delta I_4(s)\right]\\ &= \begin{bmatrix}1 & -1 & 1 & -1\end{bmatrix}\boldsymbol{\Delta I}(s),\end{aligned} \tag{57}$$

which measures the discrepancy between $(\Delta I_1+\Delta I_3)$ and $(\Delta I_2+\Delta I_4)$.

And, the transfer function of the augmented I controller for the compensating loop is,

$$G_{\mathrm{compen},i}(s) = \frac{(\Delta Z_h)_{\mathrm{sp,compen},i}(s)}{E_{\mathrm{couple}}(s)} = \frac{k_{\mathrm{compen},i}}{s}, \tag{58}$$

where $k_{\mathrm{compen},i}$ is the integral gain for the compensating loop with $k_{\mathrm{compen},1} = -k_{\mathrm{compen},2} = k_{\mathrm{compen},3} = -k_{\mathrm{compen},4} = K_{\mathrm{compen}}$ due to the symmetry and K_{compen} is the compensating coefficient. We observe from (55) that positive change in $(\Delta Z_h)_{\mathrm{sp},1}$ leads to negative change in E_{couple}, so that $K_{\mathrm{compen}} > 0$ is necessary for the compensating loop to eliminate E_{couple}.

Importantly, the floating-gap setpoint should incorporate both the I controller for the power loop and the augmented I controller for the compensating loop as,

$$(\Delta \boldsymbol{Z_h})_{\mathrm{sp}}(s) = G_I(s)\boldsymbol{E_I}(s) + \boldsymbol{G_{compen}}(s)E_{\mathrm{couple}}(s), \tag{59}$$

which is expended as,

$$\begin{aligned}(\Delta \boldsymbol{Z_h})_{\mathrm{sp}}(s) &= \frac{k_I}{s}\left[(\Delta \boldsymbol{I})_{\mathrm{sp}}(s)-\Delta\boldsymbol{I}(s)\right]\\ &\quad + \frac{K_{\mathrm{compen}}}{s}\begin{bmatrix}1\\-1\\1\\-1\end{bmatrix}\begin{bmatrix}1\\-1\\1\\-1\end{bmatrix}^T\Delta\boldsymbol{I}(s)\\ &= \frac{k_I}{s}(\Delta\boldsymbol{I})_{\mathrm{sp}}(s) + \frac{\boldsymbol{B}}{s}\Delta\boldsymbol{I}(s),\end{aligned} \tag{60}$$

where $\boldsymbol{B}$ is the coefficient matrix of the I controller for the coupled loop (*including the power loop and the compensating loop*), involving two functions: (i) the power loop to maintain I_i at I_{norm}, and (ii) the compensating loop to eliminate the current discrepancy among the four electromagnets.

In order to prevent the coupled loop from affecting the transient dynamics of the distance loop, the time constant of the coupled loop should be at least 10 times larger than that of the distance loop in the tolerable ranges as,

$$T_{\mathrm{coupled-loop}} \geq 10T_{\mathrm{distance-loop}}. \tag{61}$$

Moreover, the characteristic equation for the block diagram in Fig. 13 is calculated from (56) and (60) as,

$$|s\boldsymbol{I} - \boldsymbol{AB}| = 0, \tag{62}$$

where matrix $\boldsymbol{AB}$ is calculated as,

$$\begin{aligned}\boldsymbol{AB} &= -\frac{k_I k_P I_{eq}}{k_P Z_{h,eq}+I_{eq}}\begin{bmatrix}1&0&0&0\\0&1&0&0\\0&0&1&0\\0&0&0&1\end{bmatrix}\\ &\quad + \left[K_{\mathrm{compen}} - \frac{k_I k_P Z_{h,eq}}{4\left(k_P Z_{h,eq}+I_{eq}\right)}\right]k_P\begin{bmatrix}1&-1&1&-1\\-1&1&-1&1\\1&-1&1&-1\\-1&1&-1&1\end{bmatrix}\\ &= a\begin{bmatrix}1&0&0&0\\0&1&0&0\\0&0&1&0\\0&0&0&1\end{bmatrix} + b\begin{bmatrix}1&-1&1&-1\\-1&1&-1&1\\1&-1&1&-1\\-1&1&-1&1\end{bmatrix},\end{aligned} \tag{63}$$

where the two coefficients are $a = -k_I k_P I_{eq}/\left(k_P Z_{h,eq}+I_{eq}\right)$ and $b = k_P\left[K_{\mathrm{compen}} - k_I k_P Z_{h,eq}/4\left(k_P Z_{h,eq}+I_{eq}\right)\right]$.

Furthermore, the poles of the characteristic equation in (62) are solved as,

$$\begin{cases} s_1 = s_2 = s_3 = a = -\frac{k_I k_P I_{eq}}{k_P Z_{h,eq}+I_{eq}} < 0 \\ s_4 = a + 4b = k_P\left(4K_{\mathrm{compen}} - k_I\right)\end{cases}. \tag{64}$$

Hence, the stability criterion for the coupled loop requires $s_4 < 0$ which leads to,

$$K_{\mathrm{compen}} > k_I/4 = 0.00825\ \mathrm{m}/(\mathrm{A}\cdot\mathrm{s}). \tag{65}$$

Nevertheless, the time constants corresponding to s_1, s_2, and s_3 are identical with $T_{\mathrm{power-loop}}$ in (29) and fulfill the

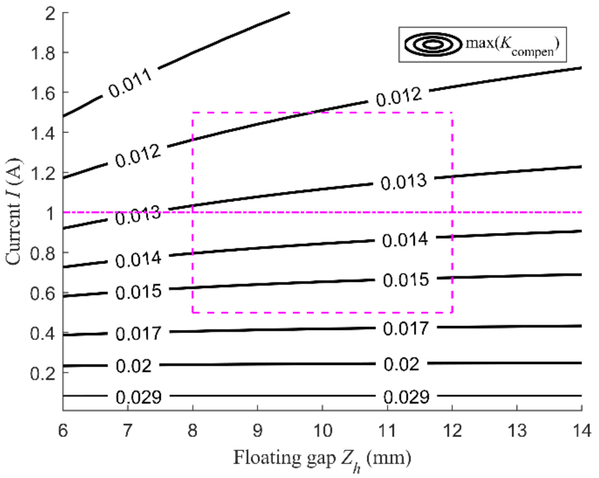

FIGURE 14. **Contour of max (K_{compen}) in the limit ranges with $k_P = -350$ A/m and $k_I = 0.033$ m/ (A · s). The magenta dashed rectangle denotes the tolerable ranges, whereas the magenta dashed-dotted line denotes I_{norm}.**

requirement in (61) already. Besides, the time constant corresponding to s_4 is,

$$T_{\text{coupled-loop},4} = -\frac{2\pi}{\left(4K_{\text{compen}} - k_I\right) k_P} \geq 10T_{\text{distance-loop}}, \tag{66}$$

which gives,

$$K_{\text{compen}} < \frac{k_I}{4} - \frac{\pi}{20T_{\text{distance-loop}} k_P}. \tag{67}$$

Fig. 14 visualizes the variation of $\max\left(K_{\text{compen}}\right) = \left(\frac{k_I}{4} - \frac{\pi}{20T_{\text{distance-loop}} k_P}\right)$ in the limit ranges with $k_P = -350$ A/m and $k_I = 0.033$ m/ (A · s). We observe that $K_{\text{compen}} = 0.011$ m/ (A · s) fulfils both requirements in (65) and (67) for the whole tolerable ranges.

It is worth mentioning that the analytical derivation for the augmented I controller in (56) assumes the same equilibrium for the four electromagnets. Hence, the derived compensating coefficient for the compensating loop, i.e., $k_I/4 < K_{\text{compen}} < \left[k_I/4 - \pi/\left(20T_{\text{distance-loop}} k_P\right)\right]$, needs to be further verified for the twisting-mode deflection. Also, Secs. III-D.2 and III-D.3 present the numerical simulation for the coupled robust constant-power-control algorithm under the twisting-mode deflection in (44).

D. NUMERICAL SIMULATION

1) CURRENT-COUPLING TEST

The current coupling among the four electromagnets is derived in Sec. III-B and verified in this subsection by imposing a ramp change in the floating-gap setpoint on P_1. Specifically, $(\Delta Z_h)_{\text{sp},1}$ ramps up with a speed of 5 mm/s since 0.05 s and maintains at 2 mm since 0.45 s as,

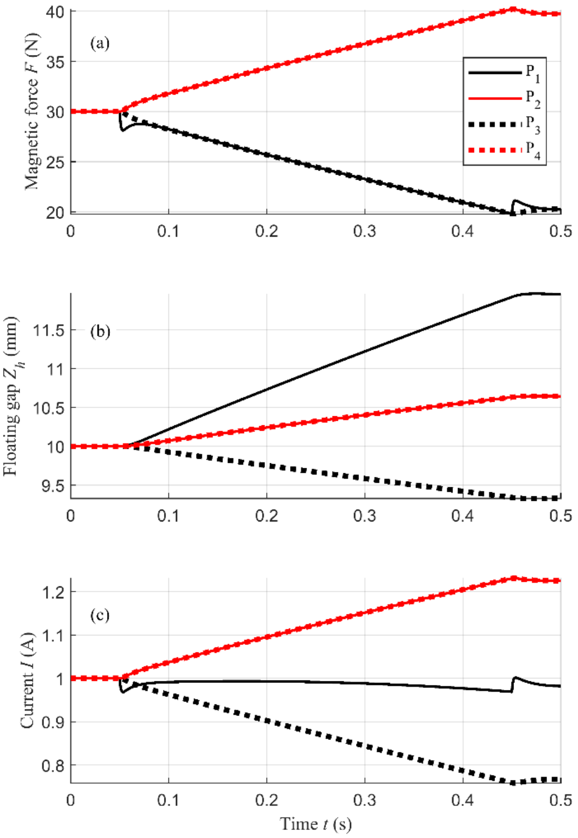

FIGURE 15. **Dynamic responses of the current-coupling test on the rigid quadruple EMS vehicle with the distance loop only, (a) magnetic force, (b) floating gap, and (c) excitation current.**

TABLE 2. **Steady-state Values of ΔI_i and $\Delta Z_{h,i}$ by analytical derivation and by numerical simulation under current-coupling test with $\delta\left(\Delta Z_h\right)_{\text{sp},1} = 2$ mm.**

Symbol	P_1	P_2	P_3	P_4
Analytical ΔI_i (A)	0.0350	0.2450	-0.2450	0.2450
Numerical ΔI_i (A)	0.0180	0.2248	-0.2326	0.2248
Analytical $\Delta Z_{h,i}$ (mm)	2.1000	0.7000	-0.7000	0.7000
Numerical $\Delta Z_{h,i}$ (mm)	1.9546	0.6436	-0.6689	0.6436

$$\left(\Delta Z_h\right)_{\text{sp},1} = \begin{cases} 0 \text{ mm}, & 0.05 \text{ s} > t \geq 0 \text{ s} \\ 5\left(t - 0.05\right) \text{ mm}, & 0.45 \text{ s} > t \geq 0.05 \text{ s} \\ 2 \text{ mm}, & t \geq 0.45 \text{ s} \end{cases}. \tag{68}$$

Fig. S2 (in supplementary materials) shows the corresponding MATLAB Simulink program for the current-coupling test on the rigid quadruple EMS vehicle only with the PD controller for the distance loop ($k_P = -350$ A/m and $k_D = -6.5$ A · s/m). Also, Figs. 15 and 16 show the dynamic responses and the $I - Z_h$ trajectories for the four electromagnets, respectively. As derived in (53)-(54), ΔI_2, ΔI_4, $\Delta Z_{h,1}$, $\Delta Z_{h,2}$, and $\Delta Z_{h,4}$ increase with the increase of $\left(\Delta Z_h\right)_{\text{sp},1}$, whereas ΔI_3 and $\Delta Z_{h,3}$ decrease. Particularly, ΔI_1 is negligible comparing with the other three ΔI_i.

Moreover, Table 2 compares the steady-state values of ΔI_i and $\Delta Z_{h,i}$ from the analytical derivation in (53)-(54) with

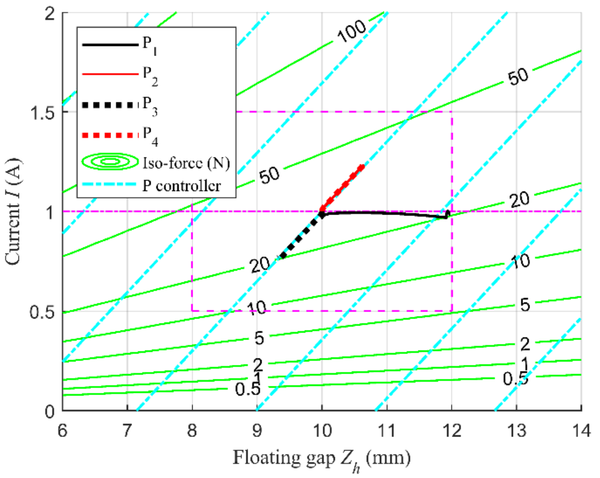

FIGURE 16. **$I - Z_h$ trajectories of the current-coupling test on the rigid quadruple EMS vehicle with the distance loop only. The iso-force curves indicate the magnitudes of the magnetic force, whereas the P-controller lines indicate the dominant transient dynamics.**

those from the numerical simulation. In Table 2, the two sets of results are consistent with each other, and the less-than-10% discrepancies result from the nonlinearity near the nominal equilibrium. Hence, the current coupling derived in Sec. III-B is verified.

2) COMPENSATING-COEFFICIENT TEST

The compensating-coefficient, K_{compen}, for the augmented I controller is verified in this subsection by imposing a ramp change in deflections on P_1 and P_3. Specifically, ee_1 and ee_3 ramp up with a speed of 10 mm/s since 0.05 s and maintains at 2.5 mm since 0.3 s as,

$$\begin{cases} ee_2 = ee_4 = 0 \\ ee_1 = ee_3 = \begin{cases} 0\text{ mm}, & 0.05\text{ s} > t \geq 0\text{ s} \\ 10\,(t-0.05)\text{ mm}, & 0.3\text{ s} > t \geq 0.05\text{ s} \\ 2.5\text{ mm}, & t \geq 0.3\text{ s}. \end{cases} \end{cases} \tag{69}$$

As derived in Sec. III-A, a twisting-mode deflection results in nontrivial changes in $Z_{h,i}$ and I_i for the four electromagnets.

Fig. S3 (in supplementary materials) shows the MATLAB Simulink program for the rigid quadruple EMS vehicle with the distance loop ($k_P = -350$ A/m and $k_D = -6.5$ A · s/m), the power loop ($k_I = 0.033$ m/ (A · s)), and the compensating loop (various K_{compen}). Moreover, the Gain switches between the single-loop scenario (Gain $=$ 0) and the coupled-loop scenario (Gain $=$ 1). Specifically, five compensating coefficients are tested for the coupled robust constant-power-control algorithm, including $K_{\text{compen}} = 0.0085, 0.0095, 0.011, 0.015, 0.05$ m/ (A · s).

Furthermore, Figs. 17 and 18 show the dynamic responses and the $I - Z_h$ trajectories for the four electromagnets respectively under the six cases, including a single-loop scenario and five K_{compen}. We observe that the single-loop scenario converges to an equilibrium with two different excitation currents, i.e., (11.20 mm, 1.42 A) and (8.70 mm, 0.54 A), whereas the five coupled-loop scenarios converge to an equilibrium with the four electromagnets at I_{norm}, i.e., (11.48 mm, 1.0 A) and (8.98 mm, 1.0 A). Hence, I_i are much closer to the tolerable range for the rigid quadruple EMS vehicle without the coupled controller, which may undermine the robustness under additional disturbances.

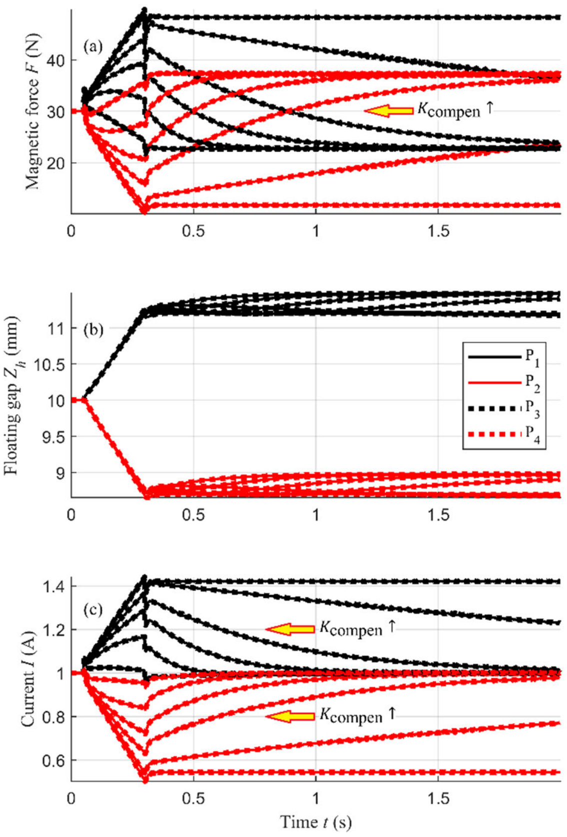

FIGURE 17. **Dynamic responses of the compensating-coefficient test on the rigid quadruple EMS vehicle for the single-loop scenario and the coupled-loop scenarios with $K_{\text{compen}} = 0.0085, 0.0095, 0.011, 0.015, 0.05$ m/ (A · s), (a) magnetic force, (b) floating gap, and (c) excitation current.**

Nevertheless, when K_{compen} decreases and approaches to 0.00825 m/(A·s) in (65), the time constant of the coupled loop increases and approaches to infinity, as implied by (66). Contrarily, when K_{compen} increases and approaches to 0.05 m/(A·s), the coupled loop has a decreasing time constant and significantly distorts the transient dynamics of the distance loop. Consequently, the coupled robust constant-power-control algorithm with $K_{\text{compen}} = 0.011$ m/ (A · s) is verified to be effective in stabilizing the rigid quadruple EMS vehicle without affecting the transient dynamics of the distance loop.

3) ROBUSTNESS TEST

In order to compare the robustness of the two scenarios, including the single-loop scenario (Gain $=$ 0, $k_P = -350$ A/m, and $k_D = -6.5$ A · s/m) and the coupled-loop

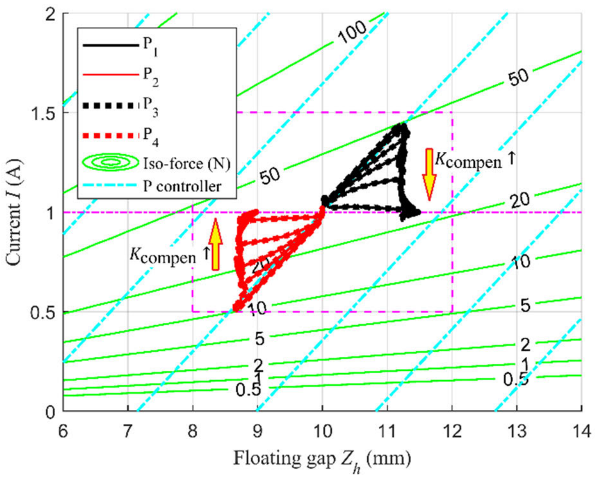

FIGURE 18. $I - Z_h$ **trajectories of the compensating-coefficient test on the rigid quadruple EMS vehicle for the single-loop scenario and the coupled-loop scenarios with** $K_{\text{compen}} = 0.0085, 0.0095, 0.011, 0.015, 0.05\ \text{m}/(\text{A}\cdot\text{s})$**. The iso-force curves indicate the magnitudes of the magnetic force, whereas the P-controller lines indicate the dominant transient dynamics.**

scenario (Gain = 1, $k_P = -350\ \text{A/m}$, $k_D = -6.5\ \text{A}\cdot\text{s/m}$, $k_I = 0.033\ \text{m}/(\text{A}\cdot\text{s})$, and $K_{\text{compen}} = 0.011\ \text{m}/(\text{A}\cdot\text{s})$), the rigid quadruple EMS vehicle is simulated with two imposed disturbances, (i) ramp changes in the guideway deflections on P_1 and P_3 and (ii) sinusoidal force disturbances on P_1 and P_2, as follows.

- The ramp changes in the guideway deflections as described in (69) are imposed on P_1 and P_3.
- The sinusoidal force disturbances are imposed on P_1 and P_2 with different orientations. $F_{\text{d},1}$ and $F_{\text{d},2}$ have the frequency of 20 rad/s (or a period of 0.31 s) and their amplitude ramps up with a rate of 40 N/s since $t = 1.5$ s as,

$$\begin{cases} F_{\text{d},1} = -F_{\text{d},2} = \text{ramp}(t)\sin(20t) \\ \text{ramp}(t) = \begin{cases} 0\ \text{N}, & 1.5\ \text{s} > t \geq 0\ \text{s} \\ 40(t-1.5)\ \text{N}, & t \geq 1.5\ \text{s}. \end{cases} \end{cases} \tag{70}$$

Figs. 19-22 show the dynamic responses and the $I - Z_h$ trajectories for the four electromagnets respectively under the two scenarios. The transient dynamics for the two scenarios during 0 s to 1.5 s have been discussed in Sec. III-D.2, and this subsection targets on the respective robustness under the sinusoidal force disturbances.

As shown in Fig. 19, the loss of control for the single-loop scenario occurs at $t = 2.46$ s (after 3.1 cycles of the sinusoidal force disturbance) when both I and Z_h of P_2 exceed the respective limit ranges; as shown in Fig. 21, the loss of control for the coupled-loop scenario occurs at $t = 3.08$ s (after 5.1 cycles of the sinusoidal force disturbance). In other words, the surviving time for the coupled-loop scenario under the sinusoidal force disturbances is 65% longer than that of the single-loop scenario.

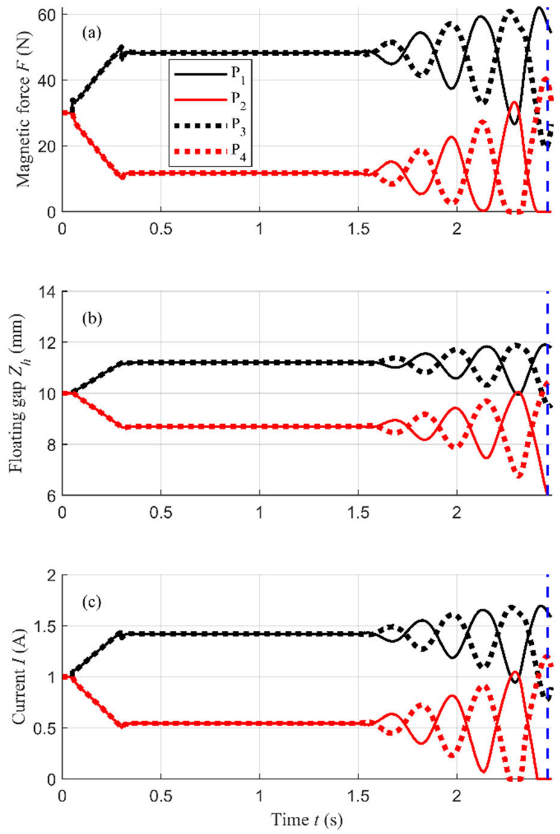

FIGURE 19. Dynamic responses of the robustness test on the rigid quadruple EMS vehicle for the single-loop scenario, (a) magnetic force, (b) floating gap, and (c) excitation current. The loss of control occurs at $t = 2.46$ **s, when both** I **and** Z_h **of** P_2 **exceed the respective limit ranges.**

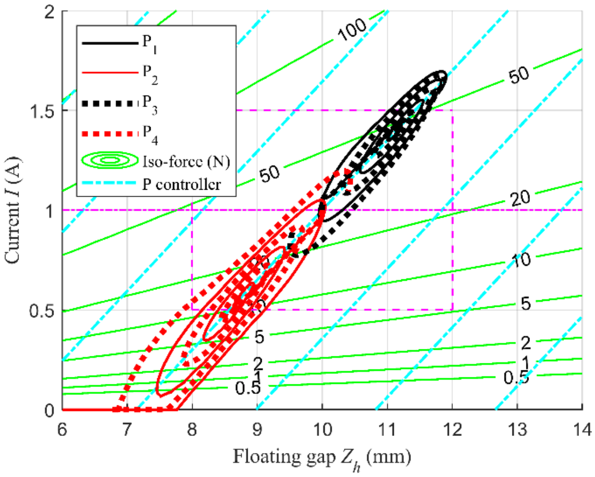

FIGURE 20. $I - Z_h$ **trajectories of the robustness test on the rigid quadruple EMS vehicle for the single-loop scenario. The iso-force curves indicate the magnitudes of the magnetic force, whereas the P-controller lines indicate the dominant transient dynamics.**

As shown in Fig. 20, the four $I - Z_h$ trajectories of the single-loop scenario concentrate in a narrow band near the P-controller line, i.e., $(I - I_{\text{norm}}) = -k_P\left(Z_h - Z_{h,\text{norm}}\right)$; as shown in Fig. 22, the four $I - Z_h$ trajectories of the

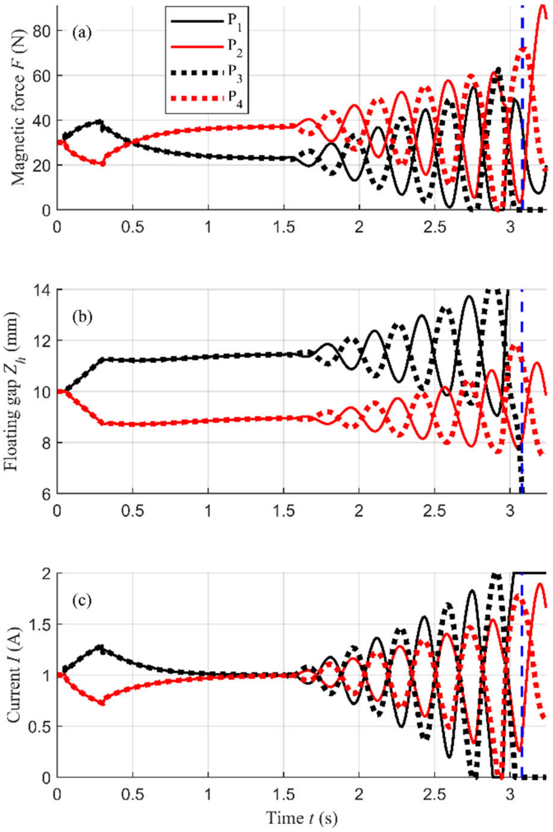

FIGURE 21. Dynamic responses of the robustness test on the rigid quadruple EMS vehicle for the coupled-loop scenario, (a) magnetic force, (b) floating gap, and (c) excitation current. The loss of control occurs at $t = 3.08$ s, when both I and Z_h of P$_3$ exceed the respective limit ranges.

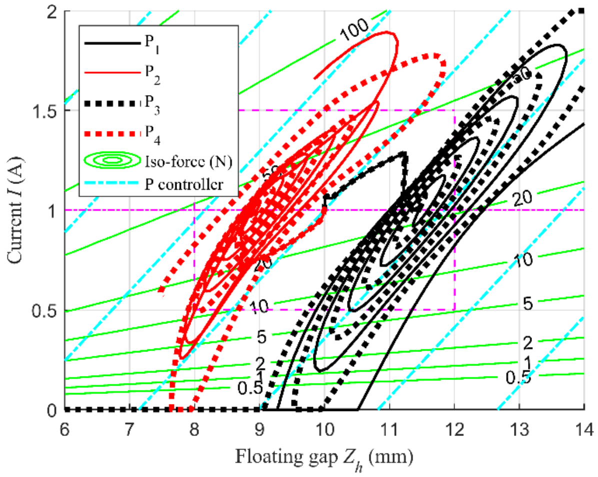

FIGURE 22. $I - Z_h$ trajectories of the robustness test on the rigid quadruple EMS vehicle for the coupled-loop scenario. The iso-force curves indicate the magnitudes of the magnetic force, whereas the P-controller lines indicate the dominant transient dynamics.

coupled-loop scenario fluctuate around I_{norm} and cover a much larger area in the limit ranges. Hence, the coupled-loop scenario delays the loss of control by maintaining the average values of I_i at I_{norm}.

Consequently, the coupled constant-power-control algorithm maximizes the controlling capability for the limit range of I and significantly enhances the robustness of the rigid quadruple EMS vehicle.

IV. CONCLUSION

This work proposes the coupled robust constant-power-control algorithm for the rigid quadruple EMS vehicle to make full use of the excitation current under both low-frequency and high-frequency disturbances. The algorithm consists of three coupled controllers, including the PD controller for the distance loop, the I controller for the power loop, and the augmented I controller for the compensating loop. Technically, the PD controller and the I controller can be determined by the single-DoF EMS system, whereas the augmented I controller is determined w.r.t. the current coupling of the rigid quadruple EMS vehicle and resolves the so-called statically indeterminate problem. Detailed modelling and analytical derivation are presented to determine the four parameters of the proposed algorithm, including k_P, k_D, k_I, and K_{compen}. Moreover, the numerical simulations are conducted with the MATLAB Simulink, and the simulation results verify the effectiveness and the outstanding robustness of the proposed algorithm. Overall speaking, the coupled robust constant-power-control algorithm involves only four parameters and is so simple that plenty of room is available for intelligent control algorithms, e.g., the optimal control, the gain-scheduling control, and the self-adaptive control. Nevertheless, the proposed algorithm sheds light on the intelligent EMS transportation system for more industrial applications.

APPENDIX

In Sec. III-A, the mass of the rigid bogie is neglected compared with the four electromagnets in order to focus on the interactions between the guideway and the four electromagnets. This appendix aims to discuss the influence from the bogie mass on the kinetics analysis and the current coupling of the rigid quadruple EMS vehicle.

For the kinetics analysis, denote the mass of the rigid bogie as M, the gravity center at $P_B = (x_B, y_B, z_B)$, the moments of inertia about the x-axis and the y-axis as $J_{xx,B}$ and $J_{yy,B}$, respectively.

Hence, the force balance of the bogie in (36) is updated as,

$$F_1 + F_2 + F_3 + F_4 = (4m + M)(g + a_B). \tag{71}$$

Moreover, the moment balance of the bogie in (37) is updated as,

$$\begin{cases} \frac{L}{2}(F_1 + F_2 - F_3 - F_4) - y_B M g = \left(J_{xx} + J_{xx,B}\right)\frac{d^2\theta_B}{dt^2} \\ \frac{W}{2}(-F_1 + F_2 + F_3 - F_4) - x_B M g = \left(J_{yy} + J_{yy,B}\right)\frac{d^2\varphi_B}{dt^2}. \end{cases} \tag{72}$$

Under the steady-state condition, combining (71) and (72) leads to,

$$\begin{cases} F_1 = F_3 + \left(\frac{y_B}{L} - \frac{x_B}{W}\right) Mg \\ F_2 = F_4 + \left(\frac{y_B}{L} + \frac{x_B}{W}\right) Mg \\ F_1 + F_2 = (2m + 0.5M)\, g + \frac{y_B}{L} Mg \end{cases}, \tag{73}$$

which implies that $F_1 = F_3$ and $F_2 = F_4$ are simultaneously established only when both $x_B = 0$ and $y_B = 0$ are established. Hence, without loss of generality, we assume $F_1 \neq F_3$ and $F_2 \neq F_4$. Therefore, the four electromagnets are floating at different equilibrium points, i.e., $\left(I_{eq,i}, Z_{h,eq,i}\right)$ with i= 1, 2, 3 and 4.

For the current coupling, as a result of different equilibriums for the four electromagnets, the analytical derivation in Sec. III-B becomes imprecise from (49) and inevitably influences the setup of the augmented I controller, which is highlighted at the end of Sec. III-C.

Practically, we can engineer $x_B \ll W$ and $y_B \ll L$, and (73) becomes,

$$\begin{cases} F_1 = F_3 \\ F_2 = F_4 \\ F_1 + F_2 = F_3 + F_4 = (2m + 0.5M)\, g \end{cases}, \tag{74}$$

which leads to the same equilibrium for the four electromagnets. Therefore, by regarding the equilibrium as the new nominal equilibrium, we can repeat the analytical derivation in this work to setup the coupled robust constant-power-control algorithm for the rigid quadruple EMS vehicle.

REFERENCES

[1] P. Leng, Y. Li, D. Zhou, J. Li, and S. Zhou, "Decoupling control of maglev train based on feedback linearization," *IEEE Access*, vol. 7, pp. 130352–130362, 2019, doi: 10.1109/ACCESS.2019.2940053.

[2] Z. G. Liu, Z. Q. Long, and X. L. Li, *Maglev Trains: Key Underlying Technologies* (Tracts in Mechanical Engineering), 1st ed. Germany: Springer, 2015.

[3] H.-W. Lee, K.-C. Kim, and J. Lee, "Review of maglev train technologies," *IEEE Trans. Magn.*, vol. 42, no. 7, pp. 1917–1925, Jul. 2006, doi: 10.1109/TMAG.2006.875842.

[4] J. S. Park, J. S. Kim, and J. K. Lee, "Robust control of maglev vehicles with multimagnets using separate control techniques," *KSME Int. J.*, vol. 15, no. 9, pp. 1240–1247, Sep. 2001, doi: 10.1007/bf03185664.

[5] S. H. Lee, H. K. Sung, J. T. Lim, and Z. Bien, "Self-tuning control of electromagnetic levitation systems," *Control Eng. Pract.*, vol. 8, no. 7, pp. 749–756, Sep. 2000, doi: 10.1016/S0967-0661(00)00005-8.

[6] P. K. Sinha and A. N. Pechev, "Nonlinear H∞ controllers for electromagnetic suspension systems," *IEEE Trans. Automat. Contr.*, vol. 49, no. 4, pp. 563–568, Apr. 2004, doi: 10.1109/TAC.2003.822865.

[7] X. Su, X. Yang, P. Shi, and L. Wu, "Fuzzy control of nonlinear electromagnetic suspension systems," *Mechatronics*, vol. 24, no. 4, pp. 328–335, Jun. 2014, doi: 10.1016/j.mechatronics.2013.08.002.

[8] A. Suebsomran, "Adaptive neural network control of electromagnetic suspension system," *Int. J. Robot. Autom.*, vol. 29, no. 2, pp. 144–154, 2014, doi: 10.2316/Journal.206.2014.2.206-3728.

[9] W.-J. Kim, S. Verma, and H. Shakir, "Design and precision construction of novel magnetic-levitation-based multi-axis nanoscale positioning systems," *Precis. Eng.*, vol. 31, no. 4, pp. 337–350, Oct. 2007, doi: 10.1016/j.precisioneng.2007.02.001.

[10] T. Mizuno, M. Takasaki, D. Kishita, and K. Hirakawa, "Vibration isolation system combining zero-power magnetic suspension with springs," *Control Eng. Pract.*, vol. 15, no. 2, pp. 187–196, Feb. 2007, doi: 10.1016/j.conengprac.2006.06.001.

[11] R. Pizá, J. Salt, A. Sala, and Á. Cuenca, "Hierarchical triple-maglev dual-rate control over a profibus-DP network," *IEEE Trans. Control Syst. Technol.*, vol. 22, no. 1, pp. 1–12, Jan. 2014, doi: 10.1109/TCST.2012.2222883.

[12] M. H. A. Yaseen, "A comparative study of stabilizing control of a planer electromagnetic levitation using PID and LQR controllers," *Results Phys.*, vol. 7, pp. 4379–4387, Jan. 2017, doi: 10.1016/j.rinp.2017.11.007.

[13] S.-Y. Cho, W.-H. Kim, I.-S. Jang, D.-W. Kang, and J. Lee, "Robust zero power levitation control of quadruple hybrid EMS system," *J. Electr. Eng. Technol.*, vol. 8, no. 6, pp. 1451–1456, Nov. 2013, doi: 10.5370/jeet.2013.8.6.1451.

[14] J. J. Cruz, A. Bittar, E. A. Costa, and R. M. Sales, "Control and optimization of the electromagnetic suspension operation of a maglev vehicle," *Presented at the 17th Int. Congr. Mech. Eng.*, Spain, 2003, pp. 150–158.

[15] T. Mizuno and Y. Takemori, "A transfer-function approach to the analysis and design of zero-power controllers for magnetic suspension systems," *Electr. Eng. Jpn.*, vol. 141, no. 2, pp. 67–75, Aug. 2002, doi: 10.1002/eej.10049.

[16] M. Morishita and T. Azukizawa, "Zero power control of electromagnetic levitation system," *Electr. Eng. Jpn.*, vol. 108, no. 3, pp. 111–120, 1988, doi: 10.1002/eej.4391080313.

[17] T. C. Wang and Y.-K. Tzeng, "A new electromagnetic levitation system for rapid transit and high speed transportation," *IEEE Trans. Magn.*, vol. 30, no. 6, pp. 4734–4736, Nov. 1994, doi: 10.1109/20.334205.

[18] Y.-K. Tzeng and T. C. Wang, "Dynamic analysis of the maglev system using controlled-PM electromagnets and robust zero-power-control strategy," *IEEE Trans. Magn.*, vol. 31, no. 6, pp. 4211–4213, Nov. 1995, doi: 10.1109/20.489929.

[19] T. Mizuno and H. Bleuler, "Self-sensing magnetic bearing control system design using the geometric approach," *Contr. Eng. Pract.*, vol. 3, no. 7, pp. 925–932, Jul. 1995, doi: 10.1016/0967-0661(95)00075-6.

[20] Z. Zhang, T. Gao, Y. Qin, J. Yang, and F. Zhou, "Numerical study for zero-power maglev system inspired by undergraduate project kits," *IEEE Access*, vol. 8, pp. 90316–90323, 2020, doi: 10.1109/ACCESS.2020.2994128.

[21] Y. Li, D. Zhou, P. Cui, P. Yu, Q. Chen, L. Wang, and J. Li, "Dynamic performance optimization of electromagnetic levitation system considering sensor position," *IEEE Access*, vol. 8, pp. 29446–29455, 2020, doi: 10.1109/ACCESS.2020.2972341.

[22] S. Banerjee, D. Prasad, and J. Pal, "Design, implementation, and testing of a single axis levitation system for the suspension of a platform," *ISA Trans.*, vol. 46, no. 2, pp. 46–239, Apr. 2007, doi: 10.1016/j.isatra.2006.09.001.

[23] M. G. Yoon and J. H. Moon, "A simple analog controller for a magnetic levitation kit," *Int. J. Eng. Res. Technol.*, vol. 5, no. 3, pp. 94–97, Mar. 2016, doi: 10.17577/IJERTV5IS030113.

ZEYI ZHANG received the bachelor's and Ph.D. degrees from The University of Hong Kong, in 2014 and 2018, respectively. He is currently a Vice Professor with the School of Electrical Engineering and Automation, Jiangxi University of Science and Technology. His research interests include permanent maglev and automatic control.

• • •